AAS 23-118

LEVERAGING THE ELLIPTIC RESTRICTED THREE-BODY PROBLEM FOR CHARACTERIZATION OF MULTI-YEAR EARTH-MOON L_2 HALOS IN AN EPHEMERIS MODEL

Beom Park* **and Kathleen C. Howell†**

While many dynamical structures in the Circular Restricted Three-Body Problem (CR3BP) serve as useful approximations to the motion of a spacecraft within a higher-fidelity ephemeris model (HFEM), a subset of the Earth-Moon L_2 halo orbit family is known to display a more dispersed behavior in the HFEM. Leveraging a consistent numerical transition method from the CR3BP to the HFEM, the Earth-Moon L_2 halo family within the HFEM is characterized by producing multi-year HFEM counterparts, highlighting the region where the transition process is particularly challenging. To gain deeper insights into the behavior of HFEM analogs, the Elliptic Restricted Three-Body Problem (ER3BP) is employed. The analysis demonstrates the formulation of HFEM solutions in the vicinity of the ER3BP Quasi-Periodic Orbits (QPOs). However, it is also observed that the ER3BP QPOs face issues in the continuation procedure, particularly in the region where HFEM transitioning presents challenges. Potential dynamical factors contributing to the observed behavior for the ER3BP QPOs are discussed, shedding light on the problematic region for HFEM transitioning.

INTRODUCTION

The future of space exploration includes a focus on the Earth-Moon L_2 halo orbit family and the nearby dynamical regime. Structures that remain bounded for a sufficient duration are leveraged for various science objectives, supporting multiple missions currently in operation. Such examples include JAXA's EQUilibriUm Lunar-Earth point 6U Spacecraft (EQUULEUS)[1] and NASA's Cislunar Autonomous Positioning System Technology Operations and Navigation Experiment (CAPSTONE) mission,[2] where bounded trajectories that utilize halo orbital structures are integrated into the trajectory design process. Moreover, the 9:2 Near Rectilinear Halo Orbit (NRHO) is envisioned to serve as the baseline trajectory for the Gateway mission.[3] Understanding the natural bounded motion of the spacecraft in the vicinity of the Earth-Moon L_2 halo family is crucial for enabling flexible and efficient future missions that are tailored to specific objectives.

The Earth-Moon Circular Restricted Three-Body Problem (CR3BP) is leveraged extensively to describe the dynamics in the Earth-Moon L_2 halo orbit region. In 1973, Farquhar and Kamel[4] compute bounded orbits utilizing the Lindstedt-Poincaré method that also incorporates additional perturbations from the lunar orbital eccentricity and solar gravity. Ignoring these perturbations, Periodic Orbits (POs) are produced by Breakwell and Brown,[5] also discovering the NRHOs near the Moon. This analysis is extended by Howell[6] for different mass ratios for the two gravitational bodies that comprise the CR3BP. More recently, Zimovan-Spreen, Howell, and Davis[7] characterize the stability information and bifurcations into nearby higher-period dynamical structures in the vicinity of NRHOs. Quasi-Periodic Orbits (QPOs) within the CR3BP are also leveraged to extend the potential options for producing a bounded spacecraft motion. Such examples are highlighted in McCarthy and Howell[8] as well as Lujan and Scheeres[9] to characterize the QPO families emanating from the L_2 halo family.

*Ph.D. Student, School of Aeronautics and Astronautics, Purdue University, West Lafayette, IN 47907; park1103@purdue.edu
†Hsu Lo Distinguished Professor of Aeronautics and Astronautics, School of Aeronautics and Astronautics, Purdue University, West Lafayette, IN 47907; howell@purdue.edu

While the POs and QPOs within the framework of the CR3BP are, in theory, indefinitely bounded, counterparts of these structures within a more accurate Higher-Fidelity Ephemeris Model (HFEM) are not guaranteed to possess the same property. Various numerical schemes are employed to generate analogs that remain bounded over a finite, yet sufficiently long, time span. Lian et al.[10] and Dei Tos and Topputo[11] leverage the multi-dimensional frequency information from the HFEM to generate bounded halo substitutes within the HFEM that span a few decades. However, this approach is only demonstrated for the halo orbits that are far from the NRHO region. Currently, resources to describe the long-term behavior of NRHO substitutes within the HFEM are relatively limited. An example of a reference Gateway baseline trajectory illustrates the construction of a 15-year solution by leveraging the 9:2 NRHO, where intermediate maneuvers are introduced and reduced in the targeting process to produce such a long-duration solution.[12] Furthermore, Davis et al.[13] note that a subset of the halo family displays a significantly more dispersed behavior within the HFEM, corresponding to an "intermediate" region where the orbits are sorted according to their perilune radii. Long-term counterparts within the HFEM for this intermediate region are not discussed in the literature. Consequently, there exists a knowledge gap regarding the *global* behavior of the ballistic long-term counterparts for these orbits within the HFEM.

The focus of this investigation is an examination of multi-year counterparts for the L_2 halo orbits within the HFEM across the entire family. Initially, the analogs are constructed utilizing halo orbits from the CR3BP as an initial guess. The L_2 halo family is divided into three separate regions based on their behavior in terms of the HFEM substitutes, with special attention to the intermediate region where transitioning poses significant challenges. This problematic region serves as an interesting case study, as similar challenges possibly exist within various regions across cislunar space and different systems, e.g., the Sun-Earth system, when transitioning the lower-fidelity structures from the CR3BP to HFEM. Thus, in a broader context, examining this challenging region within the Earth-Moon L_2 halo family aids in understanding and developing a transition process that preserves the desired characteristics from lower-fidelity models to the higher-fidelity models suitable for flight. To analyze the behavior of the substitutes within the HFEM, the investigation explores the Elliptic Restricted Three-Body Problem (ER3BP). While several intermediate models incorporate time-dependent perturbation components into the CR3BP,[14–16] Park and Howell[17] note that the most dominant perturbations for the Earth-Moon L_2 halo family emanate from the realistic pulsation of the Earth-Moon system, associated with the sidereal frequency. As such, the ER3BP is selected due to its capability to model significant changes in the Earth-Moon distance with a frequency that is close to the sidereal frequency.[17] Previous investigations that leverage the ER3BP[18,19] in this region mainly focus on the ER3BP POs. The current work also extends the framework to the ER3BP QPOs for a more comprehensive description of the evolution of the CR3BP L_2 halo orbits under the pulsation of the Earth-Moon distance. The analysis deduces that the multi-year counterparts of the HFEM are indeed constructed in the vicinity of the ER3BP structures, enabling an efficient characterization of the solution behavior within the HFEM. Leveraging the Hamiltonian structures and their continuation behavior within the ER3BP provides additional insights into the intermediate region where the transition from the CR3BP to HFEM is particularly challenging.

DYNAMICAL MODELS

The current investigation utilizes three dynamical models: CR3BP, ER3BP, and HFEM. The differential equations for each model are reviewed, with common assumptions introduced. In all models, the spacecraft is assumed to have no influence on the celestial bodies' motion, and the celestial bodies are modeled as point masses. The gravitational parameters for the bodies are defined consistently with JPL's ephemerides, DE440.bsp,[20] denoted as $\tilde{\mu}$ with subscripts E, M, and S for Earth, the Moon, and the Sun, respectively.

Regardless of the model, the trajectories in the current work are consistently visualized in the pulsating-rotating frame, also denoted as the rotating frame. The origin of the frame is located at the barycenter of Earth and the Moon (primaries) and the unit vectors $\hat{x}, \hat{y}, \hat{z}$ are defined as follows: $\hat{x}$ is always directed from Earth to the Moon, $\hat{z}$ is parallel to the angular momentum vector of the primaries, and $\hat{y}$ completes a dextral triad. The Earth-Moon distance within the rotating frame is always normalized to unity. The locations of Earth and the Moon within the rotating frame are fixed on the $\hat{x}$-axis at $\left[-\mu, 0, 0\right]^\intercal$ and $\left[1-\mu, 0, 0\right]^\intercal$, respectively. Here, $\mu = \tilde{\mu}_M/(\tilde{\mu}_E + \tilde{\mu}_M)$ and the superscript $\intercal$ denotes the transpose of a vector or matrix. Note that,

within the ER3BP and HFEM, the Earth-Moon distance is constantly pulsating. Regardless of the instantaneous dimensional distance between the primaries as described by the respective model, the locations for the primaries are fixed within the *pulsating*-rotating frame. As a result, the frame itself pulsates to consistently represent the non-dimensional Earth-Moon distance as unity in the presence of time-varying dimensional Earth-Moon distances. The non-dimentional position vector for the spacecraft within the frame is denoted as $\vec{r} = x\hat{x} + y\hat{y} + z\hat{z}$.

Circular Restricted Three-Body Problem (CR3BP) The CR3BP comprises Earth, the Moon, and the spacecraft. In an inertial frame, the primaries orbit their mutual barycenter in circular paths with a radius of l_*, known as the characteristic length. The characteristic time $t_* = \sqrt{l_*^3/(\tilde{\mu}_E + \tilde{\mu}_M)}$, is then defined accordingly. Within the rotating frame, the spacecraft motion is governed by following non-dimenional equations of motion,

$$\frac{d^2\vec{r}}{dt^2} = -2\hat{z} \times \frac{d\vec{r}}{dt} + \nabla\Omega_C, \tag{1}$$

where the independent variable for the CR3BP is denoted as t, representing the non-dimensional time. The pseudo-potential function of the CR3BP is defined by $\Omega_C = (x^2 + y^2)/2 + \Omega$, where $\Omega = (1-\mu)/r_{Es} + \mu/r_{Ms}$, and r_{Es} and r_{Ms} represent the non-dimensional distance between the Earth and the spacecraft and between the Moon and the spacecraft, respectively. The cross produced is represented as $\times$.

Elliptic Restricted Three-Body Problem (ER3BP) The ER3BP incorporates conic motion for the primaries. The true anomaly of the Moon with respect to Earth is represented by f, serving as the independent variable for the ER3BP. The eccentricity of the conic orbit is denoted as e. The motion of the spacecraft is governed by the following equations within the pulsating-rotating frame,

$$\frac{d^2\vec{r}}{df^2} = -2\hat{z} \times \frac{d\vec{r}}{df} + \nabla\Omega_E. \tag{2}$$

Here, Ω_E is the pseudo-potential function for the ER3BP, evaluated as $\Omega_E = \frac{1}{1+e\cos f}\Omega_C - \frac{e\cos f}{1+e\cos f} \cdot \frac{z^2}{2}$. Note that when e is zero, the ER3BP reduces to the CR3BP. While various values for e are utilized, Park and Howell[17] suggest that values between 0.05 and 0.055 typically represent realistic Earth-Moon motion. In the current work, $e = 0.055$ is selected to reflect a realistic value.

Higher-Fidelity Ephemeris Model (HFEM) In the current work, the HFEM incorporates three celestial bodies: Earth, the Moon, and the Sun. The ephemerides for these bodies are obtained from DE440.bsp. The spacecraft motion within the Moon-centered ECLIPJ2000 inertial frame, under the gravitational influence of these celestial bodies, is described by the following dimensional equations of motion,

$$\frac{d^2\vec{R}}{dT^2} = -\frac{\tilde{\mu}_M}{R^3}\vec{R} + \sum_{p=E,S} \tilde{\mu}_i\left(\frac{\vec{R}_{sp}}{R_{sp}^3} - \frac{\vec{R}_{Mp}}{R_{Mp}^3}\right), \tag{3}$$

where $\vec{R}$ denotes the dimensional, inertial position of the spacecraft with respect to the Moon, where the magnitude is denoted as R. The independent variable T represents the dimensional time in seconds that governs the HFEM dynamics. The perturbing bodies are represented as p, where only Earth (E) and the Sun (S) are included as such bodies in this analysis. Then, $\vec{R}_{sp}$ and $\vec{R}_{Mp}$ denote the position vectors directed from the spacecraft and the Moon to the perturbing body, respectively. To visualize the HFEM trajectories within the rotating frame, it is necessary to properly rotate and non-dimensionalize the inertial state $\vec{R}$ into $\vec{r}$. This process is accomplished by leveraging the following equation,

$$\vec{R} = \vec{R}_B + \boldsymbol{C}\vec{r}, \tag{4}$$

where $\vec{R}_B$ corresponds to the inertial position of the barycenter with respect to the Moon, and $\boldsymbol{C}$ is a direction cosine matrix with instantaneous directions of $\hat{x}, \hat{y}$ and $\hat{z}$ constructed with the ephemerides data. These directions are evaluated as $\hat{x} = \vec{R}_{EM}/R_{EM}$, $\hat{z} = \vec{H}/H$, where $\vec{H} = \vec{R}_{EM} \times d\vec{R}_{EM}/dT$, and $\hat{y} = \hat{z} \times \hat{x}$. Note that $\vec{R}_B$ and $\boldsymbol{C}$ are functions of the dimensional time T and require retrieval of instantaneous ephemerides quantities.

MULTI-YEAR HFEM COUNTERPARTS FOR L_2 HALO ORBITS

Earth-Moon CR3BP L_2 Halo Family

The Circular Restricted Three-Body Problem (CR3BP) exhibits two distinct L_2 halo families: northern and southern, both bifurcating from the planar L_2 Lyapunov family. This investigation primarily focuses on the southern family considering its relevance to future missions like the Gateway mission that utilizes a southern 9:2 NRHO. Since the configuration is symmetric, the insights from this investigation are expected to be applicable to the northern family. Figure 1(a) visually depicts the southern L_2 halo orbits within the Earth-Moon CR3BP, color-coded according to their corresponding periods in days. The relationships between the periods and the perilune radii for these orbits are further illustrated in Figure 1(b). It is essential to note that this investigation exclusively examines halo orbits that avoid collisions with the lunar surface for practical considerations.

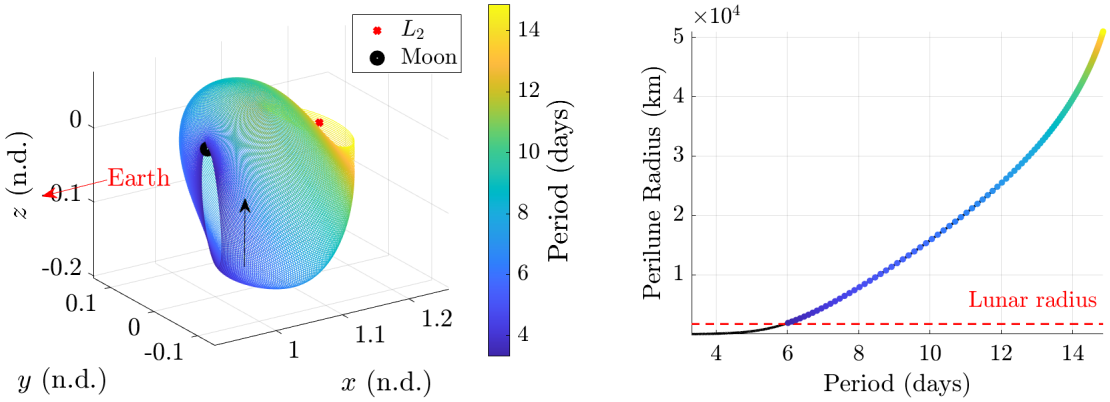

(a) Geometries within the rotating frame

(b) Perilune radii vs. period

Figure 1: Earth-Moon L_2 southern halo family

Multi-Year HFEM Ballistic Counterparts: "Unraveling" Quasi-Periodic Structures

In general, each CR3BP L_2 halo orbit ultimately yields infinite HFEM counterparts, with the specifics of the individual solutions dependent on the numerical transition process employed. This trait arises due to the underconstrained nature of the problem;[21] while the original CR3BP halo orbits are periodic, this property is not preserved within the HFEM. Consequently, the numerical targeting problem becomes underconstrained, requiring the specification of a search direction. The freedom to select this direction leads to the location of multiple, infinite HFEM analogs from the CR3BP POs.

Despite the varying details of the solutions produced through the transition process, observable patterns emerge for *sufficiently long* HFEM counterparts. Gomez et al.[22] provide relevant background on the nature of HFEM analogs, demonstrating that the Sun-Earth-Moon HFEM dynamics are reasonably approximated in terms of a quasi-periodic dynamical model. In addition to the CR3BP dynamics, this model includes a set of perturbations governed by five distinct frequencies. These quasi-periodic perturbations enable the evolution of the CR3BP POs into higher-dimensional quasi-periodic structures within the HFEM. Although the exact computation of higher-dimensional quasi-periodic structures remains challenging, as demonstrated by McCarthy,[23] Lian et al.[10] observe that over a sufficiently long time horizon, spanning several decades, the HFEM analogs reveal the existence of quasi-periodic structures governed by multiple frequencies. In light of this context, the objective here is investigation of the behavior of multi-year HFEM ballistic analogs. These multi-year counterparts are adequate for characterizing HFEM behavior, as they provide a clearer representation of the quasi-periodic nature, reducing the impact of randomness from the numerical process that is observed in short-term solutions.

Numerical Transition Process and Initial Results for HFEM Counterparts

The numerical transition process utilized in this investigation focuses on determining multi-year HFEM counterparts originating from CR3BP L_2 halo orbits. The key strategy to accomplish the evolution is to *stack* multiple revolutions of the CR3BP POs, forming longer trajectories that serve as the initial guess for the transition process. This approach relies on the assumption that quasi-periodic structures within the context of the HFEM exist in the vicinity of the stacked orbits, offering desirable starting points. To begin the transition process, the stacked trajectories are discretized into multiple patchpoint states. A targeting problem is then formulated, wherein these patchpoint states are repositioned for continuity under HFEM dynamics. This practice is common in multiple references, including Oguri et al.[1] and Bosanac et al.[24] As previously mentioned, the loss of the periodicity constraint within the HFEM creates a crucial step to specify the search direction during the targeting process. One possible approach is defining a cost function and pairing it with an optimizer to determine the search direction that optimizes the cost. This cost function may incorporate, for instance, the desired characteristics of the original solutions, such as the apse angle and time of flight. However, in the current investigation, a minimum-norm approach is preferred over an optimizer due to its computational efficiency. The minimum-norm solver aims to minimize each step taken within the targeting scheme, reducing the deviation from the initial guess provided by the CR3BP.

The numerical formulation leveraging a minimum-norm approach is further elaborated, drawing similarities with the formulation presented in Bosanac et al.[24] Multiple CR3BP halo orbits over a desired horizon time are stacked and discretized. The i-th patchpoint state along the stack of the CR3BP POs is denoted as $\vec{r}_i$ and $\vec{v}_i$ for position and velocity within the rotating frame, respectively. The total number of patchpoints is represented by m, where $1 \leq i \leq m$. The independent variable associated with the i-th patchpoint is denoted as t_i and arranged in increasing order of time. For the reference index, ref, the time is initialized as zero, i.e., $t_{ref} = 0$. In the current investigation, the reference index is computed as $ref = (m+1)/2$, corresponding to the "innermost" patchpoint from the CR3BP stack. The next step transforms the CR3BP states and time variables at patchpoints into the HFEM dimensional quantities. For position and velocity rotation and dimensionalization, Eq. (4) is leveraged to retrieve $\vec{R}_i$ and $\vec{V}_i$, respectively. For a more detailed discussion on the derivative of Eq. (4), refer to Park and Howell.[17] The HFEM independent variable T_i, corresponding to t_i, is retrieved as,

$$T_i = \int_{t_{ref}}^{t_i} \sqrt{\frac{R_{EM}^3(T)}{\tilde{\mu}_E + \tilde{\mu}_S}} dt, \tag{5}$$

where R_{EM} corresponds to the instantaneous dimensional Earth-Moon distance. Note that T_i is the dimensional time measured from the user-specified fixed reference epoch, JD_{fix}. Thus, $T_{ref} = 0$. The integration time between the $(i+1)$-th and i-th patchpoints is computed as $\Delta T_i = T_{i+1} - T_i$ for $1 \leq i \leq m-1$. The epoch associated with each patchpoint state is $JD_i = JD_{ref} + T_i/3600/24$, representing the Julian date. Using this formulation, the initial guess for the multiple shooting algorithm is constructed as,

$$\vec{X} = \left[\vec{R}_1^\intercal, \vec{V}_1^\intercal, ..., \vec{R}_m^\intercal, \vec{V}_m^\intercal, \Delta T_1, ..., \Delta T_{m-1}, JD_1, ..., JD_m\right]^\intercal, \tag{6}$$

where dividing T_i into the propagation time (ΔT) and epoch (JD) often results in a more robust configuration. The constraint is then formulated as,

$$\vec{F} = \left[\vec{F}_{state}^\intercal, \vec{F}_{epoch}^\intercal, \vec{F}_{ref}^\intercal\right]^\intercal. \tag{7}$$

The subscript "state" denotes the state continuity, ensuring that the propagated states from the i-th patchpoint coincide with the $(i+1)$-th patchpoint state for both position and velocity components. This formulation corresponds to a forward propagation, where backward propagation in time may also be leveraged.[13] Similarly, the subscript "epoch" represents the following epoch continuity constraint, $JD_{i+1} = JD_i + \Delta T_i$. The "ref" subscript corresponds to the reference epoch constraint, where $JC_{ref} = JD_{fix}$. Under this formulation, the length of $\vec{X}$ is $8m-1$, whereas the length of $\vec{F}$ is $7m-6$, illustrating the underconstrained nature of the

problem. Here, the minimum norm approach specifies the search direction through the following iterative update steps,

$$\vec{X}_{j+1} = \vec{X}_j - \boldsymbol{J}^\intercal(\boldsymbol{J}\boldsymbol{J}^\intercal)^{-1}\vec{F}_j, \tag{8}$$

where $\vec{X}_{j+1}$ represents the updated solution at the $(j+1)$-th iteration, while $\vec{X}_j$ is the current solution at the j-th iteration. The matrix $\boldsymbol{J}$ is the Jacobian of the constraint vector $\vec{F}$ with respect to the free variable vector $\vec{X}$, evaluated at $\vec{X}_j$. Note that the number of columns in the Jacobian matrix is greater than the number of rows. Consequently, the minimum norm approach allows the determination of a search direction that minimizes the step size at each iteration. Specifically, it aims to minimize the norm of $\Delta X_j := \vec{X}_{j+1} - \vec{X}_j$ while satisfying the constraint $\boldsymbol{J}\Delta X_j = -\vec{F}_j$. Although the above formulation is presented in dimensional units for illustrative purposes, it is common practice to non-dimensionalize the variables using characteristic quantities from the CR3BP, i.e., l_* (length) and t_* (time), to maintain consistent scaling properties. This transition scheme is labelled "direct," signifying that no intermediate steps are involved between the CR3BP POs and the HFEM solutions.

In accordance with this strategy, the CR3BP halo orbits visualized in Figure 1(a) are transitioned to the HFEM. The numerical formulation involves employing five patchpoints per CR3BP orbit, with a reference epoch set on $JD_{fix} = 09/23/2023$. Convergence is achieved when the non-dimensional norm of $\vec{F}$ falls below a tolerance value $1 \cdot 10^{-10}$, ensuring accurate solutions. Initially, constructing 20-year analogs is attempted, representing the maximum horizon time explored in this study. However, in cases where the targeter fails to converge within a specified maximum number of iterations, set to be 30, the horizon time is reduced. Consequently, five different horizon times are investigated, progressing from 20 years to 10 years, 5 years, 3 years, and finally 1 year. While there are no fixed criteria to define "multi-year" counterparts, solutions spanning 20 years often exhibit quasi-periodic behavior within the HFEM. Therefore, 20 years is selected as the maximum horizon time for this investigation. The results from the strategy using a direct approach to transition the CR3BP halo orbits to the HFEM are visually represented in Figure 2, where the vertical axis represents the horizon time achieved through the numerical process. The horizontal axis represents the period, P, of the CR3BP halos that are employed for the initial guesses. For a significant number of cases, the transition process successfully yields multi-year HFEM analogs, with a predominant horizon time of 20 years, evident from the data points clustered around the 20-year mark on the vertical axis. However, it is worth noting that certain counterparts fall within an "intermediate" region, where convergence leads to lower horizon times or even failure to converge to the minimum horizon time of one year. These specific counterparts are denoted in orange within the figure, as their horizon times drastically decrease below one year.

Based on the observed characteristics, the halo family is divided into three distinct regions: the (1) NRHO Region ($P < 8.6$ days), (2) Interface Region ($8.6 < P < 11.1$ days), and (3) Regular Halo Region ($P > 11.1$ days). Sample analogs from each region are illustrated in Figure 3. Notably, the HFEM counterparts within the NRHO and Regular Halo Regions closely align with the initial guesses from the CR3BP within the rotating frame. However, the Interface Region exhibits significantly dispersed geometries. This observation is consistent with Davis et al.,[13] who note that the HFEM analogs are associated with “less-periodic” behavior for a subset of L_2 halo orbits.

Building upon these observations, the Interface Region is defined as the region that presents challenges in transitioning CR3BP structures into the HFEM, characterized by two key features: (1) a significant drop occurs for the range of the solutions produced, and (2) even when an analog is computed, the geometries are associated with more dispersed behavior within the rotating frame. It is deduced that the initial guess from the CR3BP POs does not serve as suitable initial guess for the transition process based on the given numerical formulation. One possible explanation is that the quasi-periodic structures that exist within the HFEM deviate significantly from the CR3BP POs. Moreover, under the HFEM dynamics, the underlying quasi-periodic structures may break down, challenging the computation of bounded solutions for mulitple years. It is important to note, however, that the specific results visualized in Figure 2 may vary depending on the specifics of the numerical formulation employed, including but not limited to, (1) patchpoint placement schemes, (2) propagation directions, (3) baseline epochs, and (4) more refined search directions and step sizes.

Thus, the results serve as an illustrative experiment to demonstrate the generic trend observed in transitioning the CR3BP halos into HFEM analogs. Further investigations and refinements in the numerical methodology may provide valuable insights for specific cases and improve the robustness of the transition process.

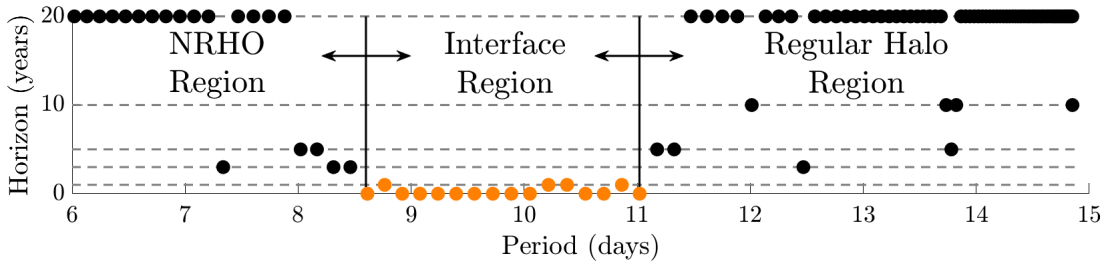

Figure 2: HFEM results with three distinct regions

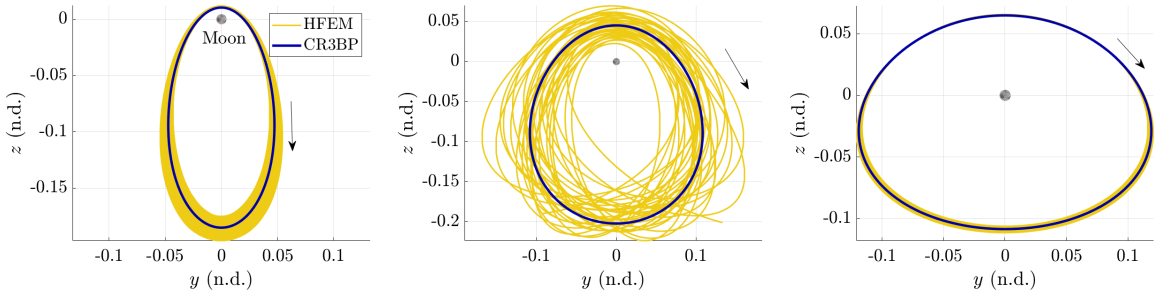

(a) NRHO Region ($P \approx 6.8$) (b) Interface Region ($P \approx 10.4$) (c) Regular Halo Region ($P \approx 14.4$)

Figure 3: Example HFEM transitioned results from each region, $\hat{y} - \hat{z}$ projection, P in days

ER3BP L_2 HALO COUNTERPARTS AND COMPARISON WITH THE HFEM

Understanding the behavior of HFEM counterparts is challenging due to their sensitivity to the specifics of the numerical transition process. This challenge leads to the exploration of periodically perturbed Hamiltonian systems that incorporate additional forces into the CR3BP in ideal forms. Specifically, the interest lies in models that predict the numerical behavior of the HFEM analogs, as demonstrated in Figure 3.

Park and Howell[17] lay the analytical foundation for selecting a suitable one-frequency Hamiltonian system within the context of transitioning CR3BP structures into the HFEM. They propose that for CR3BP orbits associated with small $\hat{y}$ excursions, such as the case for L_2 halo orbits, the realistic pulsation of the Earth-Moon distance is likely to govern the geometry change from the CR3BP POs to HFEM analogs. Consequently, the ER3BP stands out as the most desirable one-frequency model among frequently used alternatives, as it approximates the realistic pulsation with both proper magnitude and frequency. In this analysis, the global behavior of the HFEM and ER3BP counterpats across the L_2 halo family is compared to assess the HFEM long-term analogs in the vicinity of the ER3BP QPOs. Furthermore, the ER3BP is leveraged to gain deeper insights into the Interface Region, where producing long-term HFEM substitutes poses particular challenges.

The CR3BP POs generally evolve into the ER3BP counterparts as either POs or QPOs, depending on their period and any *resonance* with the period of the ER3BP system. The ER3BP renders a periodically perturbed system with a period of 2π in f (true anomaly of the Moon with respect to Earth) as given by Eq. (2). Within the f-domain, the period of the original CR3BP orbit is potentially in *resonance* when it is expressed as an integer ratio to the period of the model itself, i.e., 2π. This resonance is represented by a ratio of p:q, where p is the number of revolutions of the spacecraft along the periodic orbit and q is the number of revolutions for the Moon to complete in its conic motion around Earth during the same time interval. While resonance is defined under multiple concepts, the application here specifically denotes the resonance of the period P

with the period of the ER3BP system within the f-domain. Jorba and Villanueva[25] prove that, for sufficiently small values of e, the CR3BP POs that are *not resonant* evolve into QPOs within the ER3BP. In contrast, for resonant ratios, POs from the CR3BP generally evolve into the ER3BP POs, demonstrated numerically by multiple authors.[18,19] The numerical processes involved in computing these counterparts, i.e., QPOs and POs within the ER3BP, are detailed.

ER3BP QPO Computation

The QPOs are more globally representative of their counterparts within the ER3BP and are discussed first, given that irrational numbers are denser than rational numbers. It is known that the CR3BP POs are diffeomorphic to topological circles, i.e., any state vector on the PO may be parameterized by a single angle, θ_P, that evolves linearly with the independent variable of the system as $\theta_P = \nu_P t$. The frequency ν_P is defined as $\nu_P = 2\pi/P$, where P represents the period of the CR3BP PO.

The ER3BP QPOs in the current investigation are diffeomorphic to 2-dimensional tori, i.e., the state vector on an ER3BP QPO is parameterized by two angles, θ_P and θ_E. The longitudinal angle, θ_P, is determined as a linear function of f as $\theta_P = \nu_P f$, and similarly, the latitudinal angle, θ_E, such that $\theta_E = \nu_E f$. Importantly, ν_P remains constant between the CR3BP PO and the corresponding ER3BP QPO, noting that the ER3BP reduces to the CR3BP when eccentricity (e) is zero, and f also reduces to t. Since the ER3BP is a time-dependent system with a period of 2π with respect to f, $\nu_E = 1$. The rotation number, ρ, is defined as $\rho = \nu_E P$, representing the latitudinal angle traveled over one longitudinal period.

To compute the ER3BP QPOs, an algorithm developed by Gómez and Mondelo[26] as well as Olikara and Scheeres[27] (GMOS) is employed due to its accuracy and efficiency.[28] This algorithm employs a stroboscopic map with a fixed time interval P. At each stroboscopic time, the longitudinal angle (θ_P) remains constant and the remaining single frequency, θ_E, governs the invariant curve on the map. This curve is denoted as $\vec{u}(\theta_E)$ and represents the 6-dimensional state for the spacecraft position and velocity at the map crossing. To approximate the invariant curve, N discrete points correspond to evenly spaced angles $\theta_E \in [0, 2\pi)$ as $\theta_{E,k} = 2\pi k/N$ for $0 \leq k \leq N-1$. In the current work, $N = 51$ is leveraged. From N *guesses* for the state along the invariant curve constructed at $\theta_{E,k}$, Fourier coefficients $\vec{C}_k$ are computed via the Discrete Fourier Transform (DFT). Then, with these coefficients, the invariant curve is *approximated* as a truncated Fourier series,

$$\vec{u}(\theta_E) \approx \sum_{k=0}^{N-1} \vec{C}_k \exp\left(\mathrm{i}\theta_E k\right). \tag{9}$$

Here, "exp" corresponds to the exponential function and $\mathrm{i} = \sqrt{-1}$. Then, at the map, the state remains indefinitely on the invariant curve, where θ_E shifts by ρ for each return. This invariance condition is, then, posed as,

$$\Psi_{\theta_E}(\vec{u}(\theta_E)) = \vec{u}(\theta_E + \rho), \tag{10}$$

where Ψ_{θ_E} refers to the stroboscopic flowmap that integrates $\vec{u}(\theta_E)$ from $f = \theta_E$ to $f = \theta_E + P$. In addition to this constraint, a phase constraint is enfored on θ_P to prevent the algorithm from detecting the same QPO associated with a different θ_P value. Such formulation follows one developed by Olikara and Scheeres.[27] Thus, an iterative Newton-Raphson process is leveraged to search for N 6-dimensional states that satisfy the invariance and phase constraints.

The non-resonant CR3BP POs are expected to transform into ER3BP QPOs through two evolving parameters: (1) the eccentricity value, and (2) the period (P) associated with the underlying CR3BP PO. To track the unique QPOs as they evolve with these parameters, continuation strategies are employed in this analysis. Specifically, the continuation is accomplished in the eccentricity (e) while holding ν_P fixed, that corresponds to the vertical direction in Figure 4. This choice ensures that the rotation number (ρ) remains constant throughout the continuation process. The fixed ρ is critical to avoid landing on resonant ratios, where the QPOs cease to exist. The initial guess for the invariant curve is established utilizing a fixed point at apolune

from the CR3BP PO. Originating with a small eccentricity value $e = 1.1 \cdot 10^{-5}$, the initial invariant curve is determined to satisfy the invariance and phase constraints as previously discussed. Two different continuation strategies are then employed. The default approach utilizes a natural parameter continuation scheme, where the previously converged invariant curve is leveraged as the initial guess to compute the next invariant curve corresponding to a slightly larger e value. To reach the realistic $e = 0.055$ that is leveraged in the current work, 50 steps are employed for the natural parameter continuation scheme. The continuation process halts when the targeting process fails to converge within a predefined number of iterations (30 iterations in this case). Convergence is defined as satisfying the constraints with a tolerance of $1 \cdot 10^{-10}$ in non-dimensional units. This tolerance value aligns with previous research and ensures accurate results. To examine the global behavior of the ER3BP QPOs, multiple seeds from the CR3BP POs corresponding to different periods or ν_P are introduced, represented by the vertical columns of red dots in Figure 4. The natural parameter continuation in e is successful overall for the NRHO Region and the Regular Halo Region, as indicated in the plot. The presence of vertical gaps within these regions corresponds to the vicinity of resonant ratios, such as $4{:}1$, labelled at the top of each gap.

In the Interface Region, as defined in the HFEM investigation ($8.6 \leq P \leq 11.1$ days), the natural parameter continuation method terminates early at small values of eccentricity (e), prompting the use of an alternative continuation procedure. In this case, a pseudo-arclength continuation approach is employed, where the initial guess is provided by the tangent direction of the previously converged invariant curve. To ensure finer resolution, a non-dimensional step length of 0.001 is used, resulting in denser steps in e, as evident in Figure 4. The pseudo-arclength continuation procedure is terminated under two conditions: (1) convergence is not achieved within a predefined number of iterations, i.e., 30, or (2) a turn in the eccentricity is observed. A turn in eccentricity indicates that the pseudo-arclength continuation process naturally extends in the negative eccentricity direction at some critical e level. Such behavior may suggest the termination of the ER3BP QPO or the occurrence of bifurcation leading to other nearby QPOs. However, note that this turning behavior is rarely observed throughout the Interface Region, and it remains outside the scope of the current study.

Remarkably, the computation of QPOs faces significant challenges within the Interface Region. This region, identified during a separate numerical investigation for the HFEM counterparts, is particularly problematic for directly constructing multi-year HFEM analogs. Strikingly, this challenging region closely aligns with the region where ER3BP QPOs also encounter computational difficulties. Further discussions on this intriguing observation are provided in a later section, offering some insight on connection between the two models, i.e., the HFEM and ER3BP.

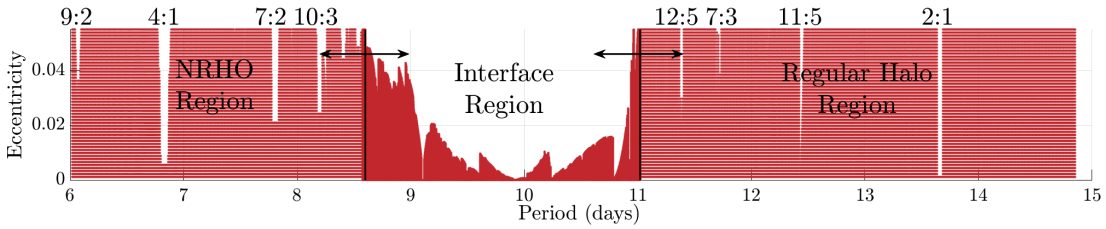

Figure 4: ER3BP QPO continuation results - the boundaries from Figure 2 are overlaid

ER3BP PO Computation

To provide a comprehensive description of the ER3BP counterparts, it is essential to detail the ER3BP POs as well. It is noted that the eigenvalues of the monodromy matrix from the CR3BP PO contain one trivial pair, denoted as $\lambda_{1,2} = 1$. As numerically demonstrated by previous authors,[18,19,29] the resonant CR3BP POs bifurcates to two ER3BP PO counterparts, where $\lambda_{1,2}$ from the CR3BP evolve into non-trivial eigenvalue pairs initially at $e = 0$ .These two ER3BP PO counterparts are labeled as A and B, respectively. Counterpart A is associated with $\lambda_{1,2}$ on the unit circle within the complex plane. On the other hand, counterpart B bifurcates to the real axis. To provide a visual example, Figure 5 highlights the $2{:}1$ ER3BP POs. Figure 5(a) displays the bifurcation of $\lambda_{1,2}$ pair as e is gradually increased from 0 to 0.055. Two ER3BP POs that

correspond to $e = 0.055$ are displayed in different views within Figures 5(b) and 5(c).

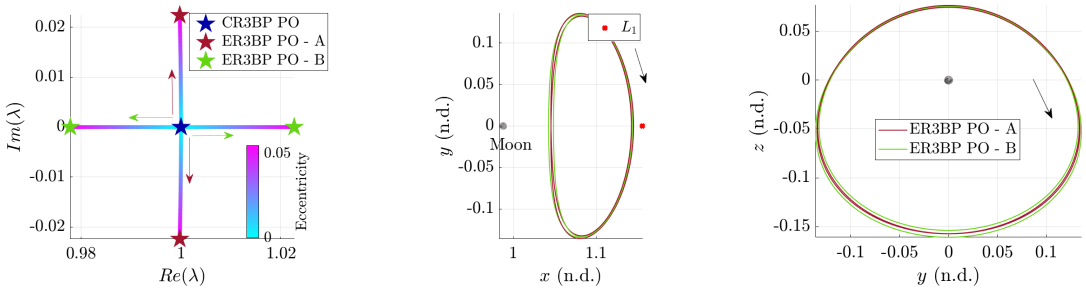

(a) Evolution of the trivial pair (b) $x - y$ plane view (c) $y - z$ plane view

Figure 5: Sample ER3BP PO with the 2:1 resonant ratio

HFEM and ER3BP Comparison - Hyperplane Examination

Based on Figures 2 and 4, it is evident that both the 20-year HFEM solutions and ER3BP QPOs are relatively well-defined within the NRHO and Regular Halo Regions. In light of this observation, the similiarities between the counterparts from the HFEM and ER3BP are investigated in these regions. For this analysis, 12 different HFEM counterparts are selected from Figure 6(a), spanning a 20-year range. These orbits are highlighted in yellow within the figure. The corresponding geometries within the rotating frame are visualized in Figure 6(b). In the pulsating-rotating frame, a hyperplane is constructed at $z = 0$ ($\dot{z} > 0$) and represented by the grey surface in the figure. Additionally, Figure 6(c) displays the ER3BP QPOs emanating from the same respective P along with the hyperplane.

The position crossings on the hyperplane from both the HFEM solutions and the ER3BP QPOs are recorded and visualized in Figure 7. Within the figures, the blue star corresponds to the crossing from the respective CR3BP PO. The comparison, not surprisingly, indicates that the HFEM crossings exhibit more complex behavior compared with the ER3BP counterparts. However, despite this difference, a noticeable similarity between the HFEM and ER3BP crossings within the NRHO and Regular Halo Regions is evident. Throughout the entire family of orbits, similar behavior is observed, not just limited to the 12 selected orbits in this analysis. Thus, it is demonstrated that the multi-year HFEM solutions are formulated in the vicinity of the ER3BP QPOs in general within the L_2 halo family.

However, in some cases, offsets in the position crossings are observed, such as in Figure 7(j), where the HFEM crossings result in higher y values compared to ER3BP counterparts. This offset is due to the lack of a phase constraint within the HFEM transition process. In contrast to the ER3BP QPO continuation process that fixes the underlying P or ρ, the HFEM targeting process does not explicitly constrain either. Rather, the targeting process locates a nearby solution that exists in the vicinity of the stacked CR3BP POs. Figure 7(l) displays a HFEM trajectory that deviates more from the ER3BP crossings. This specific case corresponds to halo orbits in the vicinity of the bifurcating Lyapunov orbit, where multiple nearby structures exist, including northern halos, Lyapunov orbits, and Lissajous orbits.[10]

HFEM and ER3BP Comparison - Fourier Analysis

The visual similarities observed within the hyperplane crossings are further supported by frequency analysis. This analysis indicates that the HFEM and ER3BP counterparts not only share similarities in their positions within the hyperplane but also exhibit common frequency structures. To conduct the Fourier analysis, multiple state samples along the analogs are collected across evenly spaced independent variables, serving as the input signal for DFT. The DFT then provides spectral domain information for the respective counterparts. Ideally, in line with Gómez et al.,[22] it is expected that the solutions within the HFEM are associated with frequencies that are linear, integer combinations of ν_P and the fundamental frequencies from HFEM itself, assuming that the multi-year HFEM analogs indeed leverage quasi-periodic structures. However, there are

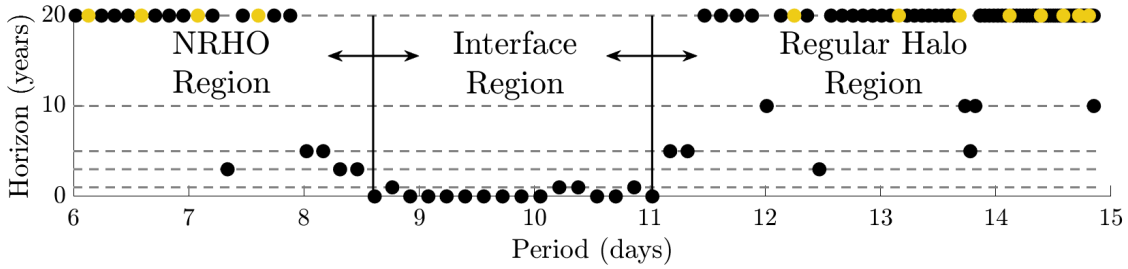

(a) Selected orbits for comparison in yellow

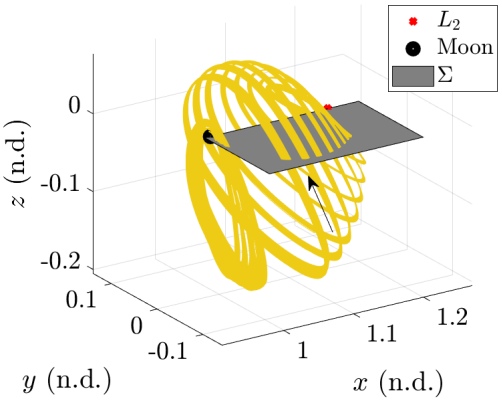

(b) Selected HFEM 20-year counterparts

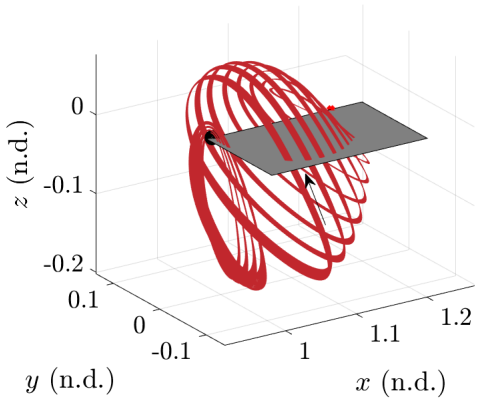

(c) Selected ER3BP QPOs

Figure 6: HFEM and ER3BP counterparts for the 12 specific orbits

certain considerations and potential challenges in this approach. Firstly, common issues encountered with DFT, such as spectral leakage, scalloping error, and aliasing, complicate the accurate detection of frequencies associated with the signal. Additionally, the HFEM analogs are not purely quasi-periodic, implying that the frequency structures potentially include some frequencies that are not explicitly modeled with the HFEM fundamental frequencies. Consequently, the frequencies observed through the DFT may not emerge as a finite number of fundamental frequencies.

Another relevant issue in the current analysis is that the dynamical models being investigated evolve with distinct independent variables. Comparing the frequency domain information requires defining a consistent independent variable to establish a common basis for comparison. To this end, the non-dimensional time variable t from the CR3BP is adopted as the common independent variable. However, determining the *isochronous correspondence* between T (HFEM) and t, and f (ER3BP) and t poses challenges as these functions are generally arbitrarily defined, potentially changing the information apparent in the frequency domain with respect to t. In this analysis, insights from Park and Howell[17] are leveraged to construct suitable functions. Note that a core property of the characteristic time within the CR3BP utilizes $t_* = \sqrt{l_*^3/(\tilde{\mu}_E + \tilde{\mu}_M)}$. Thus, the independent variable from the HFEM, T, is assumed to be correlated with t via,

$$\frac{dt}{dT} = \sqrt{\frac{\tilde{\mu}_E + \tilde{\mu}_M}{R_{EM}^3(T)}}, \tag{11}$$

where the instantaneous distance between the Earth and the Moon is leveraged to construct the instantaneous characteristic time that preserves the CR3BP property. Note that the same relationship is utilized for constructing patchpoints in the direct transition process as done for Eq. (5). Similarly, the independent variable for the ER3BP, f, and t, are related via,

$$\frac{dt}{df} = \frac{1}{\sqrt{1 + e\cos f}}, \tag{12}$$

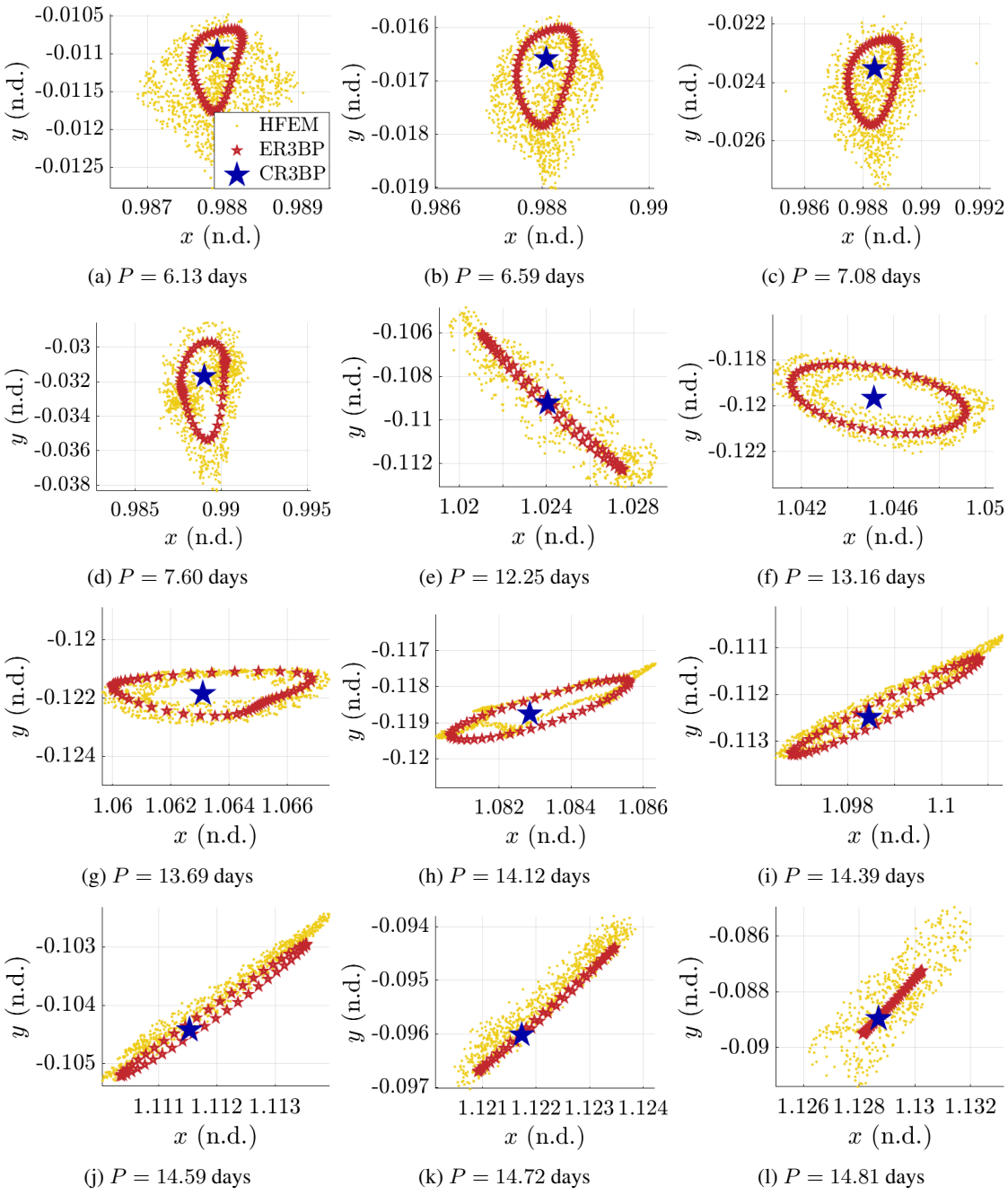

(a) $P = 6.13$ days (b) $P = 6.59$ days (c) $P = 7.08$ days

(d) $P = 7.60$ days (e) $P = 12.25$ days (f) $P = 13.16$ days

(g) $P = 13.69$ days (h) $P = 14.12$ days (i) $P = 14.39$ days

(j) $P = 14.59$ days (k) $P = 14.72$ days (l) $P = 14.81$ days

Figure 7: HFEM and ER3BP counterparts - hyperplane examination

where a conic equation is employed for derivation that also preserves the CR3BP nondimensionalization properties. For further interpretation of these isochronous correspondence functions and derivations, refer to Park and Howell.[17] Then, 2^{18} samples are collected from 20 years of CR3BP POs, ER3BP QPOs, and HFEM solutions that are evenly placed in t utilizing Eqs. (11) and (12). While all 6-dimensional state components illustrate similar behavior, the $\hat{x}$ position component is investigated in the current work as an example.

Within the common t domain, three *core* frequencies are expected to arise for the HFEM analogs. The first type of frequency is ν_C, associated with the P of the underlying CR3BP POs. While no phase constraints are introduced in the HFEM transition process, the times along the patchpoints, T_i, are constructed utilizing Eq. (5); the average "period" for the HFEM substitutes within the t-domain is expected to be near the original P from the CR3BP PO employed as the initial guess. Then, two fundamental frequencies associated with the HFEM are considered: $\nu_1 \approx 0.9896$ and $\nu_2 \approx 0.9234$, mainly associated with the pulsation of the Earth-Moon distance and the solar position within the $\hat{x} - \hat{y}$ plane, respectively. For more accurate physical interpretations of these frequencies, refer to Gómez et al.[22] The exact numbers for ν_1 and ν_2 are slightly different from the reference, as t is utilized as the independent variable here. While previous authors note the existence of three additional frequencies, the contributions from these frequencies are typically associated with lower amplitudes compared to the influence from ν_1 and ν_2, and are not considered in the current work. In short, the frequencies from the HFEM counterpart are investigated in terms of linear, integer combinations of ν_C, ν_1, and ν_2.

Similarly, from the DFT on the ER3BP QPOs, two *core* frequencies are expected. While within the f-domain, these frequencies are fixed as ν_P and $\nu_E = 1$, transforming the independent variable from f to t results in slightly different frequencies. Specifically, in the t-domain, the ER3BP QPO that originates from the CR3BP PO with ν_P is associated with $\alpha\nu_C$ and $\alpha\nu_E = \alpha$, where $\alpha \approx 0.9736 = 1/\sqrt{1+e}$ with $e = 0.055$. This value is numerically determined since Eq. (12) is an elliptic integral that does not yield a closed-form solution. Thus, for a ER3BP QPO that emanates from a CR3BP PO with ν_C, the frequency spectrum is expressed as linear, integer combinations of $\alpha\nu_C$ and $\alpha\nu_E$. Consider the frequency domain information illustrated in Figure 8(a), generated for $P \approx 14.39$ days. The horizontal axis of the plot denotes the nondimensional frequency with respect to t. The vertical axis corresponds the $\log_{10}$ of the respective amplitude. The stars denote the peaks in DFT spectra, colored differently for the CR3BP PO, ER3BP QPO, and HFEM 20-year analogs. Note that the peaks of the CR3BP trajectory correspond to $k_C\nu_P$, where k_C is a positive integer. The shape of the halo orbits in the rotating frame allows a progressive attenutation (or decay) in amplitude relative to the frequency. Note that, in the vicinity, the ER3BP and HFEM trajectories also produce peaks with similar magnitudes. Thus, the HFEM and ER3BP spectra are associated with peaks at $k_C\nu_P$ and $k_C\alpha\nu_P$, respectively. This behavior is expected, since the counterparts, in general, remain in the vicinity of the original CR3BP halos within the rotating frame.

While the HFEM spectrum demonstrates more complex behavior in general, focusing on the first few dominant frequencies provides valuable insights. Figure 8(b) provides a zoomed-in view of the lower-frequency domain, where the grey stars represent the frequencies associated with the first 10 dominant amplitudes for the HFEM results. For this specific case, these frequencies are approximated as linear combinations of ν_P, ν_1, and ν_2, i.e., $\nu \approx k_C\nu_P + k_1\nu_1 + k_2\nu_2$, where k denotes the integer coefficient for each core frequency. Table 1 provides the frequencies ordered by amplitude, and the last row corresponds to the difference between the detected frequency and the linear approximation, denoted as $\Delta\nu$.

Two observations are noteworthy from the example in Figure 8(b). First, $\nu_P \pm \nu_1$ emerge as the most dominant perturbations that cannot be expressed as multiples of ν_P. Frequencies other than $k_C\nu_C$ are indeed associated with the quasi-periodic nature of the HFEM counterparts, where the perturbations mainly originate from ν_1 and ν_2. As evident from the decaying behavior of the spectrum in Figure 8(a), the relative magnitude of lower frequencies effectively represents the order of perturbations as well. In this specific example, the perturbation originating from $\nu_P + 2\nu_2$ is only 25% compared to the perturbation from $\nu_P + \nu_1$. Second, note that the ER3BP QPO also exhibits similar amplitude levels for the same *structure* of frequencies, i.e., $\alpha\nu_P \pm \alpha\nu_E$, as shown in Figure 8(b). This observation suggests that the ER3BP QPOs share common frequency traits with the HFEM counterparts. The investigation extends across the entire family to explore the trend regarding these two behaviors.

The dominant impact from $\nu_P \pm \nu_1$ is established by examining the frequency structures associated with the first 10 dominant amplitudes across the entire family. Figure 8(c) illustrates the frequency structure for the 20-year HFEM analogs. The horizontal axis corresponds to the period P of the underlying CR3BP PO, while the vertical axis denotes the order of the amplitudes corresponding to the peaks from DFT. Different markers denote different structures for the respective frequencies, where the detected frequencies are approximated as linear combinations of ν_P, ν_1, and ν_2. In Figure 8(c), the blank spaces reflect P values where 20-year HFEM solutions are not retrieved (Figure 10), or where the detected frequency is not represented as a linear combination of ν_P, ν_1, and ν_2 within a given tolerance (set to be $0.01\nu_P$). These occurrences most often arise due to the inherent limitations of the DFT in accurately detecting frequencies, as previously discussed. However, the patterns disclosed in Figure 8(c) are deemed sufficient to illustrate the general behavior. The most dominant frequencies typically appear as $k_C\nu_P$ (■), corresponding to multiples of the underlying CR3BP PO frequency, where k_C is a positive integer. It is expected that the first dominant frequency is always $k_C\nu_P$ with $k_C = 1$, with an exception occurring near $P = 14.8$ days. This exception corresponds to the region near the bifurcating Lyapunov orbit, where the targeter may leverage various nearby structures, as also apparent from Figure 7(l). Similarly, the second dominant frequency is $2\nu_C$ for most orbits. It is noticed that $\nu_P \pm \nu_1$ (▲, ▼) usually exhibit larger amplitudes compared to other perturbing frequencies. The amplitudes originating from solar gravity (■, ■) are generally associated with smaller amplitudes across the family.

The amplitudes corresponding to $\nu_P \pm \nu_1$ (▲, ▼) and $\alpha\nu_P \pm \alpha\nu_E$ (▲, ▼) are also compared between the HFEM and ER3BP spectra. Figure 8(d) illustrates that the amplitude associated with each frequency structure displays very similar magnitudes across the two models. This observation aligns with the hyperplane examination, where the ER3BP exhibits representative behavior for the HFEM counterparts as well. The discrepancy between ν_C in the HFEM and $\alpha\nu_C$ in the ER3BP implies that ER3BP QPOs tend toward higher periods within the t-domain in general compared to the HFEM counterparts when utilizing the same CR3BP PO with period P. This behavior is evident from offset behavior observed within Figures 7(i), 7(j), and 7(k), where the HFEM counterparts often display higher y position values at the hyperplane crossings originating from the same CR3BP POs. Due to the inherent discrepancy in the independent variables utilized for the HFEM and ER3BP, the HFEM solutions do not exactly leverage the ER3BP QPOs originating from the same CR3BP PO. However, it is sufficient to conclude that, for this orbit family, the HFEM long-term analogs are formulated in the vicinity of the ER3BP QPOs, and the ER3BP structures effectively approximate the quasi-periodic structures within the HFEM.

These findings hold important implications. First, the observation aligns with the analytical results from Park and Howell,[17] where pulsation, mainly associated with ν_1, emerges as the dominant source of perturbations for L_2 halo orbits, rather than the solar gravity that is primarily associated with ν_2. The numerical investigation here confirms the validity of the formulation proposed in Park and Howell.[17] Secondly, while various periodically perturbed Hamiltonian systems exist and offer valuable insights into higher-fidelity models, it is not always clear which behavior is preserved from these intermediate models into the HFEM. The results produced through both hyperplane and frequency analyses provide a more concrete and comprehensive approach to conclude that HFEM solutions primarily rely on quasi-periodic structures resembling the ER3BP QPOs for this specific dynamical regime.

FURTHER INVESTIGATION INTO THE INTERFACE REGION

The similarity between the HFEM and ER3BP counterparts for the given orbit family motivates an investigation into the Interface Region, with a specific focus on the dynamics in the ER3BP. Notably, both the HFEM and ER3BP encounter challenges in constructing their respective counterparts within this region. The central question arises: does the failure in the ER3BP QPO continuation process reflect a fundamental dynamical limit of the QPOs, or is it merely a manifestation of numerical challenges in the employed process? To gain insight, a detailed analysis is conducted to explore potential underlying dynamical issues associated with the QPO continuation challenges.

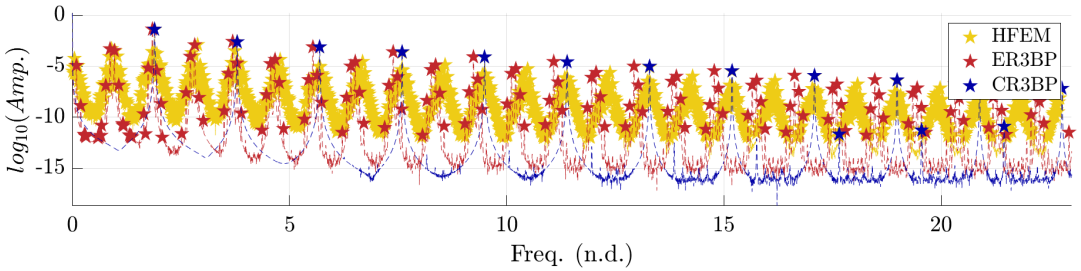

(a) Frequency information for a sample orbit, $P \approx 14.39$ days

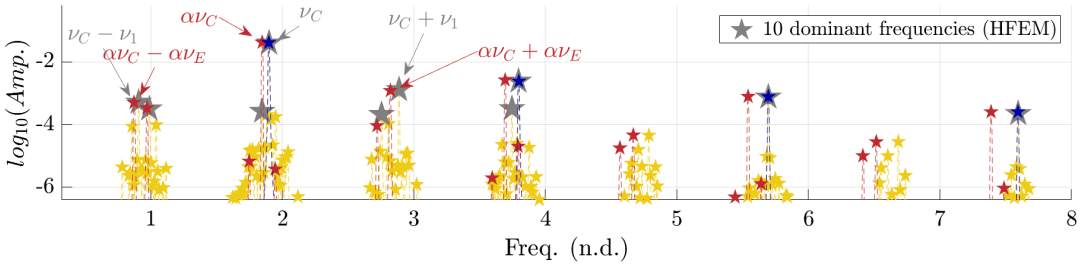

(b) Zoomed-in view near lower frequency domain for a sample orbit, $P \approx 14.39$ days

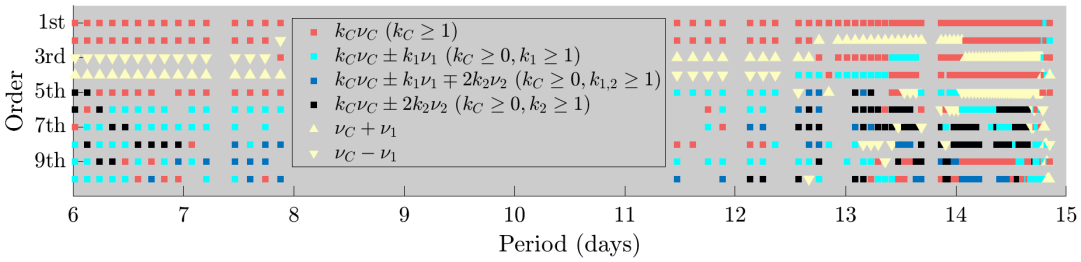

(c) Frequency structures across the L_2 halo family

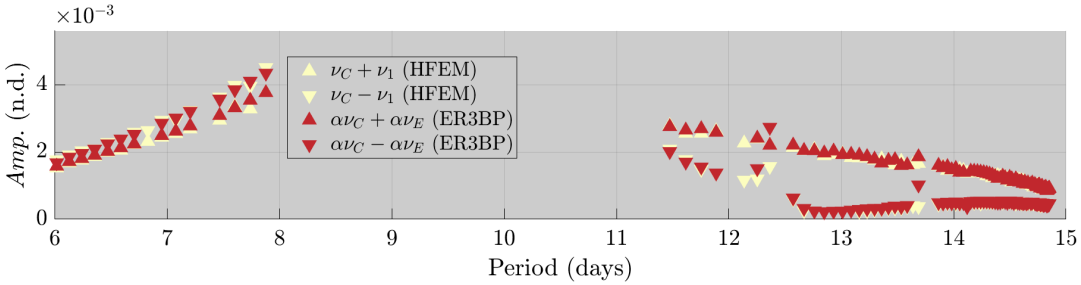

(d) Comparison between the ER3BP and HFEM across the family

Figure 8: HFEM and ER3BP counterparts - Fourier analysis

Table 1: First 10 dominant frequencies (grey stars from Figure 8(b))

Order	1st	2nd	3rd	4th	5th	6th	7th	8th	9th	10th
$Freq.$ (n.d.)	1.8994	3.7961	2.8880	5.6955	0.9081	3.7461	0.9886	1.8467	7.5949	2.7547
$log_{10}(Amp.)$ (n.d.)	-1.3940	-2.6131	-2.8859	-3.1215	-3.2858	-3.4913	-3.4993	-3.5745	-3.6499	-3.6751
k_C	1	2	1	3	1	1	0	0	4	1
k_1	0	0	1	0	-1	0	1	0	0	-1
k_2	0	0	0	0	0	2	0	2	0	2
$\Delta\nu$ (n.d.)	0.0010	0.0008	0.0000	0.0002	0.0008	0.0009	0.0010	0.0001	0.0012	0.0009

ER3BP QPO Continuation Challeges

The GMOS algorithm approximates invariant curves utilizing truncated Fourier series, where the accuracy of the approximation depends on the number of parameters employed to construct the series, i.e., N. While $N = 51$ is generally sufficient to represent the curves accurately, it is inadequate when the shape of the invariant curve becomes "complex" due to any local dynamics. In such cases, the GMOS algorithm struggles to locate the invariant curve that satisfies the invariance condition (Eq. (10)) within the specified tolerance.

One notable scenario where this behavior arises is when the rotation number ρ approaches a rational number, corresponding to a near-resonance period P. Near-resonant periods lead the invariant curve to approach the fixed points on the stroboscopic map originating from the ER3BP PO, associated with the resonant period P. Rosales et al.[30] observe that the QPOs "approach" the PO within the Bi-Circular Four-Body Problem (BCR4BP) for near resonant periods. Similar behavior is observed for the ER3BP QPOs and POs. For instance, when $P \approx 13.66$ days, corresponding to the 2:1 resonance ratio, the QPOs approaching this period encounter numerical issues, as illustrated in Figure 9. Figures 9(a) and 9(b) showcase the invariant curves for the QPOs approaching the resonant ratio from $P < 13.66$ days and $P > 13.66$ days, respectively, at the fixed eccentricity value $e = 0.055$. Visual inspection reveals that the invariant curves gradually become complex, leading to the failure of the GMOS algorithm as $N = 51$ is inadequate to accurately model the curve. Moreover, the shapes of the invariant curves also "approach" the resonant POs, encompassing both A and B counterparts within the configuration space. As the resonant period P is reached, the invariant curve is eventually destroyed. In this case, the numerical challenges stemming from the GMOS algorithm indeed arise from a dynamical origin and suggest the breakdown of the QPO structure at the exact resonant ratio.

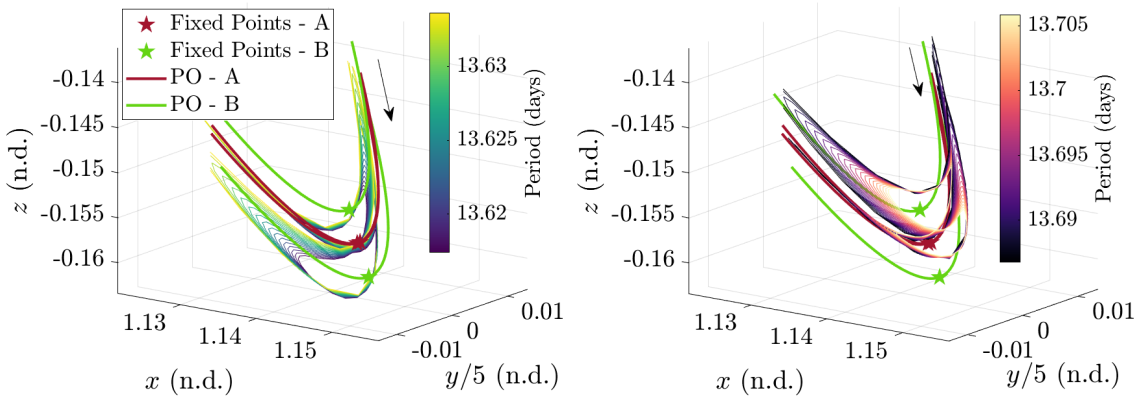

(a) $P < 13.66$ days

(b) $P > 13.66$ days

Figure 9: Invariant curves for QPOs near the 2:1 resonance, $P = 13.66$

The results for the global behavior of ER3BP QPOs within Figure 4 leveraged continuation in eccentricity. Currently, the authors are not aware of any specific dynmical limits that are previously reported in the literature. The current analysis encounters numerical challenges as $N = 51$ is eventually insufficient to accurately represent the invariant curve. The association of this phenomenon with the breakdown of the QPO motion at a certain threshold eccentricity value remains elusive; to complement the investigation, two additional numerical experiments are introduced, providing additional insights.

Nearby Bounded Motion within the ER3BP over a Long Horizon

To explore the complex shapes of the invariant curves and their potential link to the breakdown of QPO structures, an alternative test is introduced; it aims to demonstrate that the complex behavior observed for the invariant curves is not solely due to numerical artifacts. The test involves stacking multiple revolutions of the desired orbits to reveal the underlying QPO structures within the ER3BP. A targeting process, similar to the HFEM transition scheme, is devised to compute the bounded ER3BP structure over a long duration.

The process involves stacking 20 years of CR3BP POs initially. Utilizing this stacked data as the initial guess, incremental changes in eccentricity are introduced through 500 steps covering the range of $[0, 0.055]$, leading to long-term solutions corresponding to $e = 0.055$; the end states are left unconstrained here. If the continuation process fails to converge, the failing eccentricity is recorded.

Sample results for the originaing CR3BP orbit member with period $P \approx 10.67$ days, corresponding to the Interface Region where the QPO continuation process fails for some eccentricity value ($e \approx 0.0145$), are plotted in Figure 10. The last QPO before the continuation process halts is depicted in Figure 10(a). A hyperplane is then placed at $z = 0$ with a positive direction crossing, as indicated by the arrow. The velocity components along this hyperplane are illustrated in Figure 10(b), with different colors representing the eccentricity associated with each QPO as the continuatation steps proceed. Figure 10(c) displays the results from the 20-year bounded ER3BP trajectories that reveal two significant observations. Firstly, the bounded motion over an extended period leverages the underlying quasi-periodic motion available within the ER3BP model. Secondly, the continuation process fails at a similar value of eccentricity ($e \approx 0.0148$).

The same experiment is extended to mulitple cases within the Interface Region. Figure 11, where just the Interface Region is included, illustrates the results, where the blue circles correspond to the continuation failure points for the 20 year (20Y) bounded ER3BP trajectories. While some areas, mainly $P < 9$ days, exhibit minor mismatches between the results from the ER3BP QPO continuation and the 20Y results, the general boundaries formulated by the QPO continuation limits are also observed in this separate, independent numerical process. Thus, it is reasonable to conclude that a dynamical issue potentially exists, preventing the long-term bounded trajectories, as well as QPOs, from existing beyond certain eccentricity levels. The complex shape of the invariant curve is possibly indicative of such a limit, and this intriguing behavior commonly emerges within the Interface Region.

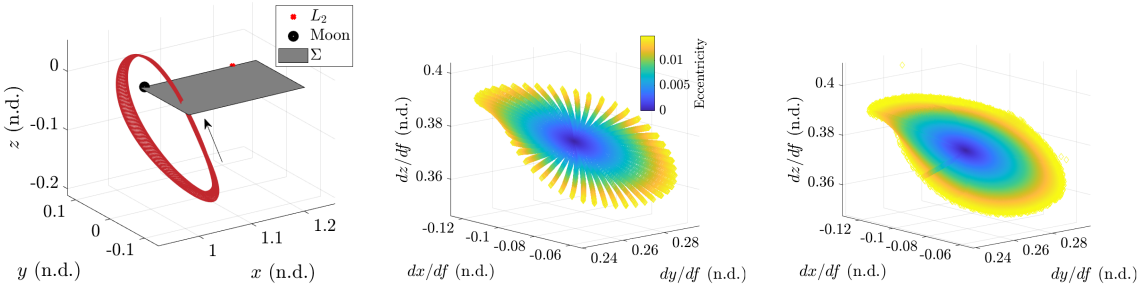

(a) Last QPO along the continuation (b) QPO: crossings at Σ (c) 20Y: crossings at Σ

Figure 10: Comparison between ER3BP QPOs and 20Y solutions for varying e, $P = 10.67$ days

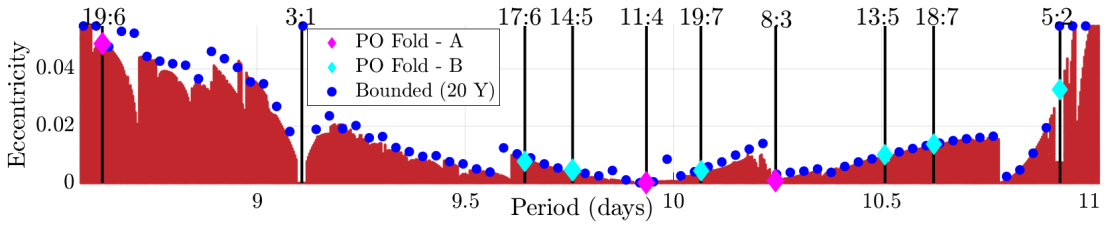

Figure 11: Boundaries from 20Y solutions and the first cyclic fold for POs

Nearby ER3BP POs and Cyclic Fold Bifurcation

For further insights, the stability properties of POs with resonant period P are investigated within the Interface Region. Sample p:q ratios are indicated as black lines in Figure 11. Note that $p \leq 19$ and $q \leq 7$ are selected as bounds to compute the periodic orbits with acceptable accuracy; as both numbers increase, the

accuracy in the propagation as well as the eigenvalue computation degrades due to longer propagation times and multiple revolutions around the Moon. Each resonant CR3BP PO is continued into the corresponding ER3BP POs, noting the existence of two counterparts, A and B.

The *cyclic fold* bifurcation is a specific type that attracts particular attention among the various bifurcations observed in this process. It is commonly present throughout the Interface Region for the investigated p:q ratios, except for 3:1. The eccentricity values at which these bifurcations occur generally align with the boundaries formulated by the QPO continuation process. A general schematic for the cyclic fold bifurcation is illustrated in Figure 12(a). Initially, a pair of eigenvalues lies on the real axis (★) or on the unit circle (★) within the complex plane. The pair then undergoes a transition through the trivial pair (★) at the exact bifurcation point, resulting in a change in the stability characteristics. While this change in stability does not always induce local extrema in eccentricity, the bifurcations that involve such turns are recorded as cyclic folds.

As an example, consider the sample pseudo-arclength continuation result for the 5:2 A PO counterpart, corresponding to the rightmost vertical black line in Figure 11. The A counterpart bifurcates from the CR3BP PO, with the trivial eigenvalue pair, $\lambda_{1,2}$, evolving onto the unit circle (★→ ★, corresponding to '1' within Figure 12(c)). Figure 12(b) depicts a hodograph with the initial x position along the PO and the corresponding eccentricity value. As the continuation process progresses as described in Figure 12(b), the eccentricity reaches a local maximum at $e \approx 0.03$. At this point, the complex pair returns to the trivial pair (★→ ★, corresponding to '2' within Figure 12(c)). Finally, the pair bifurcates to a real pair, resulting in a negative direction in the eccentricity, indicating a cyclic fold (★→ ★, corresponding to '3' within Figure 12(c)). Different behaviors are observed concerning the cyclic fold bifurcation. While, in this case, the trivial pair from the CR3BP PO bifurcates, it is possible that the other two pairs bifurcate with a turn in eccentricity. It is also observed that only one of the counterparts bifurcates in this manner or both counterparts display similar behavior, but at different eccentricity values, before reaching $e = 0.055$.

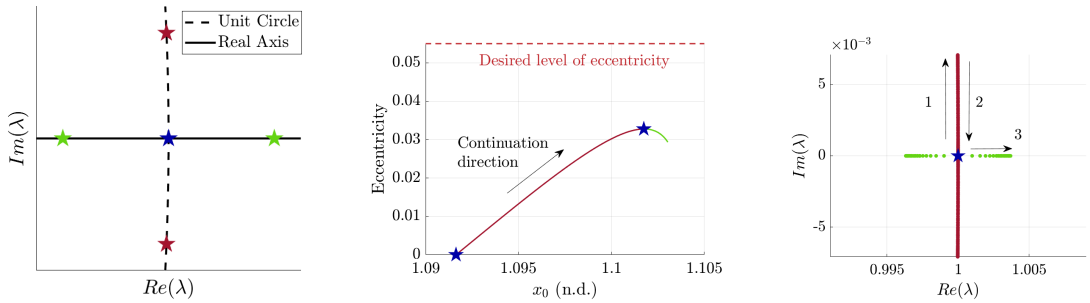

(a) Schematic for eigenvalues (b) 5:2 A continuation (c) 5:2 bifurcation

Figure 12: Cyclic fold bifurcation for 5:2 A with local extrema in e

Within the Interface Region, cyclic fold bifurcations for selected p:q resonant POs within the ER3BP are noted. The diamond markers in Figure 11 represent the minimum eccentricity value where the *first* cyclic fold is observed during the continuation of the POs within the Interface region. The bifurcation exhibits varying behavior, where either counterpart A or B bifurcates at lower eccentricities compared to each other. These cases are represented as ♦ and ♦ in the figure, respectively. Additionally, among the three eigenvalue pairs from the monodromy matrix for the ER3BP POs, no clear patterns exist in the first cyclic fold bifurcation; all three pairs are observed as demonstrating the first cyclic fold along the continuation across different POs. Despite these complexities, the first cyclic fold bifurcation eccentricity values align closely with the eccentricity boundaries located via the ER3BP QPO continuation. As the ER3BP POs turn in eccentricity, nearby QPOs possibly encounter qualitative behavior changes as well. Possible behaviors include, but are not limited to, bifurcation into nearby ER3BP QPOs emanating from the CR3BP two-dimensional tori or folding onto the same ER3BP QPO. Note that such bifurcation analysis for QPOs is extremely challenging as invariant curves become complex before reaching the exact e value where bifurcations potentially occur.

CONCLUDING REMARKS

The current work focuses on the numerical investigation of analogs for Earth-Moon Circular Restricted Three-Body Problem (CR3BP) L_2 halo orbit family within a Higher-Fidelity Ephemeris Model (HFEM). Multi-year counterparts are produced via a numerical process leveraging the CR3BP halo orbits as initial guesses, where distinct regions are identified along the halo family, highlighting an Interface Region where challenges arise in constructing long-term solutions and the converged solutions significantly deviate from the original CR3BP geometry.

For deeper insights into the behavior of the HFEM analogs, the Elliptic Restricted Three-Body Problem (ER3BP) is employed. For the entire family, the similarities between the solutions from the HFEM and Quasi-Periodic Orbits (QPOs) within the ER3BP are investigated through hyperplane examination and Fourier analysis. It is observed that the HFEM analogs are most significantly influenced by the realistic pulsation of the Earth-Moon system, with the ER3BP providing valuable estimates for this perturbed environment.

For the Interface Region that is identified from the HFEM counterparts, the ER3BP QPO construction also faces challenges as the invariant curves become more complex. Attempting to compute long-term bounded solutions for the ER3BP reveals similar boundaries, suggesting the existence of a threshold eccentricity above which long-term ER3BP solutions and QPOs perhaps cease to exist. Investigation of nearby periodic orbits focuses on the cyclic fold bifurcation, and it is determined that the eccentricity values associated with cyclic folds closely align with the boundaries formulated by the QPO and long-term bounded solutions. The behavior of multi-year HFEM analogs within the Interface Region indicates significant deviations from the CR3BP. Analysis from the ER3BP suggests that the pulsation between Earth and the Moon potentially disrupts the QPO motion within the ER3BP, leading to challenges in computing multi-year HFEM analogs as well.

Future analysis is warranted to further validate the findings from this investigation. Employing different targeting and continuation strategies for the HFEM transition could add validation for the existence of the Interface Region. Moreover, exploring alternative ER3BP QPO continuation strategies, such as continuation in the rotation number rather than eccentricity, may yield more robust results and add more understanding of the dynamical causes of the QPO computation issues. While this investigation focuses on the Earth-Moon L_2 halo family, it is crucial for future research to extend to other regions throughout cislunar space and also different systems, such as the Sun-Earth CR3BP, in order to further characterize cases where transitioning the CR3BP structures into the HFEM is particularly challenging.

ACKNOWLEDGEMENTS

The first author would like to thank Kwanjeong Educational Foundation for the financial support. Valuable discussions with past and former members from Multi-Body Dynamics Research Group, including Rohith Reddy Sanaga, Dhruv Jain, Juan-Pablo Almanza-Soto, and Brian McCarthy, are appreciated. Portions of this work are also supported by Purdue University and under Grant NASA JSC 80NSSC18M0122.

REFERENCES

[1] K. Oguri, K. Oshima, S. Campagnola, K. Kakihara, N. Ozaki, N. Baresi, Y. Kawakatsu, and R. Funase, "EQUULEUS trajectory design," *The Journal of the Astronautical Sciences*, Vol. 67, No. 3, 2020, pp. 950–976.

[2] "Advanced Space, LLC, Webpage," `https://advancedspace.com/`. Accessed: 2023-01-24.

[3] J. C. Crusan, R. M. Smith, D. A. Craig, J. M. Caram, J. Guidi, M. Gates, J. M. Krezel, and N. B. Herrmann, "Deep space gateway concept: extending human presence into cislunar space," *2018 IEEE Aerospace Conference*, IEEE, 2018, pp. 1–10.

[4] R. W. Farquhar and A. A. Kamel, "Quasi-periodic orbits about the translunar libration point," *Celestial mechanics*, Vol. 7, No. 4, 1973, pp. 458–473.

[5] J. V. Breakwell and J. V. Brown, "The 'halo' family of 3-dimensional periodic orbits in the Earth-Moon restricted 3-body problem," *Celestial mechanics*, Vol. 20, No. 4, 1979, pp. 389–404.

[6] K. C. Howell, "Three-dimensional, periodic,'halo'orbits," *Celestial mechanics*, Vol. 32, No. 1, 1984, pp. 53–71.

[7] E. M. Zimovan-Spreen, K. C. Howell, and D. C. Davis, "Near rectilinear halo orbits and nearby higher-period dynamical structures: orbital stability and resonance properties," *Celestial Mechanics and Dynamical Astronomy*, Vol. 132, No. 5, 2020, pp. 1–25.

[8] B. P. McCarthy and K. C. Howell, "Leveraging quasi-periodic orbits for trajectory design in cislunar space," *Astrodynamics*, Vol. 5, No. 2, 2021, pp. 139–165.

[9] D. Lujan and D. J. Scheeres, "Earth–Moon L2 quasi-halo orbit family: characteristics and manifold applications," *Journal of Guidance, Control, and Dynamics*, Vol. 45, No. 11, 2022, pp. 2029–2045.

[10] Y. Lian, G. Gómez, J. J. Masdemont, and G. Tang, "A note on the dynamics around the Lagrange collinear points of the Earth-Moon system in a complete solar system model," *Celestial Mechanics and Dynamical Astronomy*, Vol. 115, 2013, pp. 185–211.

[11] D. A. Dei Tos and F. Topputo, "Trajectory refinement of three-body orbits in the real solar system model," *Advances in Space Research*, Vol. 59, No. 8, 2017, pp. 2117–2132.

[12] D. Lee, "Gateway destination orbit model: A continuous 15 year NRHO reference trajectory," *White paper, NASA Johnson Space Center*, Vol. 103, 2019.

[13] D. C. Davis, S. M. Phillips, K. C. Howell, S. Vutukuri, and B. P. McCarthy, "Stationkeeping and transfer trajectory design for spacecraft in cislunar space," *AAS/AIAA Astrodynamics Specialist Conference*, 2017, pp. 1–20.

[14] M. A. Andreu, "Preliminary study on the translunar halo orbits of the real Earth–Moon system," *Celestial Mechanics and Dynamical Astronomy*, Vol. 86, 2003, pp. 107–130.

[15] K. K. Boudad, K. C. Howell, and D. C. Davis, "Dynamics of synodic resonant near rectilinear halo orbits in the bicircular four-body problem," *Advances in Space Research*, Vol. 66, No. 9, 2020, pp. 2194–2214.

[16] R. R. Sanaga and K. C. Howell, "Synodic resonant halo orbits in the Hill restricted four-body problem," *AAS/AIAA Astrodynamics Specialist Conference, American Astronautical Society, Austin, Texas*, 2023.

[17] B. Park and K. C. Howell, "Leveraging intermediate dynamical models for transitioning from the circular restricted three-body problem to an ephemeris model," *AAS/AIAA Astrodynamics Specialist Conference, American Astronautical Society, Charlotte, North Carolina*, 2022.

[18] H. Peng and S. Xu, "Stability of two groups of multi-revolution elliptic halo orbits in the elliptic restricted three-body problem," *Celestial Mechanics and Dynamical Astronomy*, Vol. 123, No. 3, 2015, pp. 279–303.

[19] F. Ferrari and M. Lavagna, "Periodic motion around libration points in the elliptic restricted three-body problem," *Nonlinear Dynamics*, Vol. 93, No. 2, 2018, pp. 453–462.

[20] R. S. Park, W. M. Folkner, J. G. Williams, and D. H. Boggs, "The JPL planetary and lunar ephemerides DE440 and DE441," *The Astronomical Journal*, Vol. 161, No. 3, 2021, p. 105, 10.3847/1538-3881/abd414.

[21] D. A. Dei Tos and F. Topputo, "Trajectory refinement of three-body orbits in the real solar system model," *Advances in Space Research*, Vol. 59, Apr. 2017, pp. 2117–2132, 10.1016/j.asr.2017.01.039.

[22] G. Gómez, J. Masdemont, and J. Mondelo, "Solar system models with a selected set of frequencies," *Astronomy & Astrophysics*, Vol. 390, No. 2, 2002, pp. 733–749.

[23] B. P. McCarthy, *Cislunar trajectory design methodologies incorporating quasi-periodic structures with applications*. PhD Dissertation, Purdue University, WestLafayette, Indiana, 2022.

[24] N. Bosanac, A. D. Cox, K. C. Howell, and D. C. Folta, "Trajectory design for a cislunar cubesat leveraging dynamical systems techniques: The lunar icecube mission," *Acta Astronautica*, Vol. 144, 2018, pp. 283–296.

[25] A. Jorba and J. Villanueva, "On the persistence of lower dimensional invariant tori under quasi-periodic perturbations," *Journal of Nonlinear Science*, Vol. 7, No. 5, 1997, pp. 427–473.

[26] G. Gómez and J. M. Mondelo, "The dynamics around the collinear equilibrium points of the RTBP," *Physica D: Nonlinear Phenomena*, Vol. 157, No. 4, 2001, pp. 283–321.

[27] Z. P. Olikara and D. J. Scheeres, "Numerical method for computing quasi-periodic orbits and their stability in the restricted three-body problem," *Advances in the Astronautical Sciences*, Vol. 145, No. 911-930, 2012, pp. 911–930.

[28] N. Baresi, Z. P. Olikara, and D. J. Scheeres, "Fully numerical methods for continuing families of quasi-periodic invariant tori in astrodynamics," *The Journal of the astronautical sciences*, Vol. 65, 2018, pp. 157–182.

[29] S. Campagnola, M. Lo, and P. Newton, "Subregions of motion and elliptic halo orbits in the elliptic restricted three-body problem," *AAS/AIAA Space Flight Mechanics Meeting*, 2008.

[30] J. J. Rosales, A. Jorba, and M. Jorba-Cuscó, "Families of halo-like invariant tori around L2 in the Earth-Moon bicircular problem," *Celestial Mechanics and Dynamical Astronomy*, Vol. 133, No. 4, 2021, p. 16.